Gondwana Research 98 (2021) 277–288

Contents lists available at ScienceDirect

Gondwana Research

journal homepage: www.elsevier.com/locate/gr

Plate motion and plume-induced subduction initiation

Marzieh Baes [a,b,*], Stephan Sobolev [b,c], Taras Gerya [d], Robert Stern [e], Sascha Brune [b,c]

[a] Institut für Geologie, Leibniz Universität Hannover, Germany
[b] GFZ German Research Center for Geosciences, Potsdam, Germany
[c] Institute of Geosciences, University of Potsdam, Potsdam, Germany
[d] Department of Earth Sciences, ETH-Zurich, Zurich, Switzerland
[e] Department of Geosciences, University of Texas at Dallas, USA

ARTICLE INFO

Article history:
Received 26 March 2021
Revised 1 June 2021
Accepted 13 June 2021
Available online 22 June 2021

Keywords:
Plume-induced subduction initiation
Plate motion
Numerical models
Plume buoyancy
Lithospheric strength

ABSTRACT

Impingement of a hot buoyant mantle plume head on the lithosphere is one of the few scenarios that can initiate a new subduction zone without requiring any pre-existing weak zones. This mechanism can start subduction and plate tectonics on a stagnant lid and can also operate during active plate tectonics where plume-lithosphere interactions is likely to be affected by plate motion. In this study, we explore the influence of plate motion on lithospheric response to plume head-lithosphere interaction including the effect of magmatic weakening of lithosphere. Using 3d thermo-mechanical models we show that the arrival of a new plume beneath the lithosphere can either (1) break the lithosphere and initiate subduction, (2) penetrate the lithosphere without subduction initiation, or (3) spread asymmetrically below the lithosphere. Outcomes indicate that lithospheric strength and plume buoyancy control plume penetration through the lithosphere whereas the plate speed has a subordinate influence on this process. However, plate motion may affect the geometry and dynamics of plume-lithosphere interaction by promoting asymmetry in the subduction zone shape. When a sufficiently buoyant plume hits a young but subductable moving lithosphere, a single-slab modern-style subduction zone can form instead of multiple subduction zones predicted by stagnant lid models. In the case of subduction initiation of older moving oceanic lithosphere, asymmetrical cylindrical subduction is promoted instead of more symmetrical stagnant lid subduction. We propose that the eastward motion of the Farallon plate in Late Cretaceous time could have played a key role in forming one-sided subduction along the southern and western margin of the Caribbean and NW South America.

1. Introduction

Subduction zones are essential components of plate tectonics and therefore understanding different subduction initiation scenarios is a natural focus of geodynamic research (e.g., Stern and Gerya, 2018; Crameri et al., 2020 and references therein). Different physical mechanisms and tectonic settings have been proposed for forming new convergent plate boundaries including: (1) spontaneous collapse of old oceanic lithosphere and its foundering into the mantle at passive margins (e.g., Wilson, 1966; Nikoloava et al., 2010), possibly assisted by the suction mantle flow (Baes and Sobolev, 2017), (2) various weakening mechanisms at passive margins such as water weakening (Regenauer-Lieb et al., 2001) and sediment loading (Cloetingh et al., 1982; 1984; 1989), (3) collapse of old oceanic plate at long lithospheric weaknesses such as transform faults or fracture zones (Stern, 2004; Toth and Gurnis, 1998; Hall et al., 2003; Gurnis et al., 2004; Baes et al., 2018), mid-oceanic ridges (Ishikawa et al., 2002; Lebrun et al., 2003) and along STEP faults (Subduction-Transform-Edge-Propagator; Baes et al., 2011a), (4) propagation of subduction along passive margins (Zhou et al., 2020), (5) subduction of young oceanic plate along passive margins induced by external converging forces (Zhong and Li, 2019; 2020), (6) subduction polarity reversal in back-arc regions as a result of congestion of a mature subduction zone by buoyant lithosphere (Baes et al., 2011b; Holt et al., 2018; Von Hagke et al., 2016), (7) Subduction zone transference (or subduction backstepping) by arc/plateau accretion (Stern, 2004; Zhong and Li, 2020; Kerr, 2003), (8) large bolide impact (Hansen, 2009; O'Neill et al., 2017) and (9) lithospheric collapse around a large, hot plume head (plume-induced subduction initiation or PISI; Ueda et al., 2008; Burov and Cloetingh, 2009; 2010; 2020a; 2020b;; Gerya et al., 2015; Baes et al., 2016). Among the above-mentioned scenarios, large bolide impact and PISI are the only ones

* Corresponding author.
E-mail addresses: baes@geowi.uni-hannover.de, baes@gfz-potsdam.de (M. Baes).

https://doi.org/10.1016/j.gr.2021.06.007
1751-7311/

which do not require a pre-existing lithospheric weakness or forces induced by plate tectonics and can initiate subduction within the single/stagnant lid (e.g., Gerya et al., 2015; Crameri and Tackley, 2016). Taking into account that large bolide impacts rapidly diminished after the Earth's formation and likely only affected geodynamics of the Hadean Earth (O'Neill et al., 2017), Gerya et al. (2015) suggested that PISI triggered the beginning of plate tectonics. Sobolev and Brown (2019) further proposed that multiple events of PISI might have dominated the tectonic regime before establishing global plate tectonics, causing episodic regional resurfacing at the Earth and producing early continental crust.

Ueda et al. (2008) investigated the impingement of a mantle plume on oceanic lithosphere using 2d numerical models. When a mantle plume head arrives beneath lithosphere, mantle melting produces a plateau above the plume head. Dykes above sufficiently big and buoyant plumes can help weaken the lithosphere and break it. Spreading of the buoyant plume rocks atop of broken segments of lithosphere together with negative buoyancy of the surrounding oceanic plate can lead to foundering of proto-slabs into the mantle to form a new subduction zone. The controlling factor in this process is the localized weakening of the lithosphere above the plume head, which depends on plume buoyancy, magmatic flux, and lithospheric strength. Burov and Cloetingh (2010) and Cloetingh et al. (2021) showed that at shallow depth intracontinental subduction initiation induced by a mantle plume is governed by lithospheric rheological stratification and free surface. Phase changes and interaction of the new subducting slab with the mantle are key factors controlling continental subduction at greater depth. Following recognition of the first evidence of plume-induced subduction initiation in the Caribbean (Whattam and Stern, 2014), Gerya et al., (2015) carried out comprehensive 3d numerical modeling to investigate plume-lithosphere interactions. Results showed that the lithospheric response to arrival of a rising mantle plume beneath the plate depends on the lithospheric strength and its age, magmatic weakening above the plume head, and lubrication of the plate interface by hydrated crust. In the early Earth, episodic lithospheric drips were likely when the plume interacted with young, weak oceanic lithosphere whereas multi-slab subduction initiated if the plume impinged on old, strong, dense lithosphere. On the present-day Earth initiation of single- or multi-slab subduction depends on several parameters, including the size, temperature, and composition of the plume, the age and brittle/plastic strength of the oceanic lithosphere and thickness of the oceanic crust (Baes et al., 2016; 2020a; 2020b). Crameri and Tackley (2016) presented the first 3d global mantle convection model with a free surface, in which plume-induced subduction was self-consistently produced. They showed that narrow mantle plumes impinging on the base of the lithosphere cause locally weak plate segments and large topography at the lithosphere-asthenosphere boundary, which can cause subduction initiation. Their model also produced a lithospheric overturn in form of rapidly retreating plume-induced subduction of an initially prescribed homogeneous stagnant lid.

In PISI, the initial step in forming a new subduction zone is penetration of the plume into the lithosphere. Plume penetration, however, does not lead to sustained subduction if the overlying oceanic lithosphere is younger than 5–10 Myr (Baes et al., 2016) or if the plume head is not large or hot enough (Gerya et al., 2015). This explains the scarcity of plume-induced subduction initiation, as most large oceanic plateaus form on oceanic lithospheres that are less than 5–10 Myr (Whittaker et al., 2015). Several tectonic features such as crustal heterogeneities, external compressional/extensional forces and pre-existing lithospheric weaknesses can further affect deformation caused by plume-lithosphere interactions. The lithospheric response to impingement of a mantle plume head also depends on position of the plume head and the plateau-oceanic crust transition (Baes et al., 2020b). Arrival of a mantle plume beneath a thick (and hence buoyant) plateau may hinder formation of a new subduction if the plume head is far away from plateau-crust transition (Baes et al., 2020a; 2020b). On the contrary, external forces can ease PISI. For instance, PISI of old oceanic lithosphere with overthickened oceanic plateau-like crust only becomes possible if it is stretched by external tectonic forces. The other facilitating factor in subduction initiation is pre-existing rheological weakness (e.g., a hydrated oceanic fracture zone) in the lithosphere (Baes et al., 2016).

So far three natural terrestrial examples of plume-induced subduction initiation have been proposed whereas further PISI examples have been suggested for Venus (e.g., Davaille et al., 2017; Gulcher et al., 2020). The first was for the southern and western margins of the Caribbean Plate (Whattam and Stern 2014). On the basis of geochemical, isotopic, geochronological, and tectonic considerations Whattam and Stern (2014) suggested that the arrival of a mantle plume head circa 100 Ma was the key factor in Late Cretaceous subduction initiation along Central America and northern South America (Supplementary Fig. S1 shows the present-day tectonic setting of the Caribbean region along with a plate reconstruction model proposed by Whattam and Stern (2014)). Interaction of lithosphere with the Galapagos plume head formed the Caribbean large igneous province and triggered lithospheric collapse to form new subduction zones along the southern and western margins of the Caribbean plate. This interpretation is supported by plate kinematic reconstructions indicating that western Caribbean subduction zones formed in an intra-oceanic environment conceivably as a result of impingement of a mantle plume on lithosphere (Boschman et al., 2019)). A second example of PISI is proposed for formation of the Cascadia subduction zone in Eocene times (Stern and Dumitru, 2019). Arrival of the Yellowstone mantle plume head beneath western North America at ~55 Ma terminated the existing Cordilleran subduction zone leading to lithospheric collapse and development of the present Cascadia subduction zone. Recently 3d mantle convection models constrained by ophiolite records of Neotethys subduction suggested that the pre-Deccan plume initiated the southern Neotethys subduction at ~110–105 Ma (Rodriguez et al., 2021).

Based on the Whattam and Stern (2014) model, the Caribbean region was subjected to at least two episodes of plume-related magmatic events since 140 Ma. An earlier episode may have occurred 140–110 Ma resulting in formation of a plateau. Whattam and Stern (2014) suggested that pre-existing compositional and density contrasts between the 140–110 Ma plateau and its surrounding normal oceanic lithosphere may have created favorable conditions for PISI on the southern margin of the Caribbean and north-west of South America at circa 100 Ma. Apparently, the Caribbean plateau is one of the few examples of a large oceanic plateau formed on oceanic lithosphere older than 10 Myr (Whittaker et al., 2015). This is a favorable condition for PISI (Baes et al., 2016). Formation of a single-slab subduction in the Caribbean might be due to either plume-plateau interaction in an extensional regime or arrival of a mantle plume beneath oceanic lithosphere with typical crustal thickness of 8 km (Baes et al., 2020a). It could be also the consequence of plume-plateau interaction when the plume head impinged on the oceanic lithosphere close to the plateau-oceanic crust transition (Baes et al., 2020b).

It has been hence demonstrated on the basis of natural data (e.g., Whattam and Stern, 2014; Stern and Dumitru, 2019) that PISI can operate during active modern-style plate tectonics where plume-lithosphere interactions are likely to be affected by plate motion. However, previous studies investigated plume-lithosphere interactions either for the case of stationary lithosphere or for moving lithosphere but ignored the effect of magmatic weakening of lithosphere above the plume head. Our aim

in this study is to use 3d numerical thermo-mechanical modeling to investigate the response of moving lithosphere to the arrival of a stationary mantle plume including the effect of magmatic lithospheric weakening. We show that under certain conditions plate motion can affect the lithospheric response to plume-lithosphere interaction.

2. Numerical modeling

2.1. Model description

We use 3d thermo-mechanical models employing the I3ELVIS code which is based on finite difference staggered grid and marker-in-cell techniques with an efficient OpenMP multigrid solver (Gerya, 2013, 2010). It solves the continuity, momentum and energy equations to obtain stresses and velocities:

$$\nabla \cdot \vec{v} = 0$$

$$\frac{\partial \sigma_{ij}}{\partial x_j} - \frac{\partial P}{\partial x_i} + \rho g_i = 0 \quad (1)$$

$$\rho C_P \left(\frac{DT}{Dt}\right) = -\nabla \cdot \vec{q} + H_r + H_a + H_s + H_l$$

where $\frac{D}{Dt}$, P, ρ, $\vec{v}$, σ_{ij}, g_i, C_P and $\vec{q}$ are Lagrangian time derivative, pressure, density, velocity, deviatoric stress tensor, gravity acceleration, heat capacity and heat flux, respectively. H_r, H_a, H_s and H_l denote for radioactive, adiabatic, shear and latent heating, respectively.

The model domain covers a volume of 1302 km × 328 km × 1302 km that is discretized to 373 × 165 × 373 grids (finer grid in vertical direction). The upper most layer of the model is 20-km thick "sticky air" with a low density (1 kg/m^3) and viscosity ($1 \times 10^{18} Pas$) to simulate surface topography (Crameri et al., 2012). Below this layer are upper crust, lower crust, mantle lithosphere and asthenosphere till depth of 328 km. A mushroom-shaped plume with different plume head radiuses in different models exists within the asthenosphere. In the reference model (model M1), the plume head radius is 140 km with a center 230 km deep. In the initial setup of the experiments (Fig. 1), the 30 km cylindrical plume tail is located below the bottom model boundary and forms as the plume rises. Plume head and plume tail are defined as mantle rocks with higher temperature compared to ambient mantle. Plume rises due to buoyancy associated with higher temperature. The upper and lower crusts are 2 km and 6 km thick layers and their rheological parameters are based on wet quartzite and plagioclase (An75) (Ranalli, 1995), respectively (Table 1). The thickness of lithosphere is 50 km, corresponding to an oceanic lithosphere with the age of 20 Myr. The ages and hence thicknesses of lithosphere are changed to investigate their effect on the model results (Table 2). The ambient mantle and plume are considered to be composed of dry olivine and wet olivine, respectively (Ranalli, 1995).

The viscosity depends on stress, temperature and pressure and is expressed as:

$$\eta_{diffusion} = 1/2 \frac{A_D}{\sigma_{cr}^{n-1}} exp\left(\frac{E+PV}{RT}\right)$$

$$\eta_{dislocation} = 1/2 A_D^{1/n} exp\left(\frac{E+PV}{nRT}\right) \dot{\varepsilon}_{II}^{(1-n)/n} \quad (2)$$

$$\frac{1}{\eta_{effective}} = \frac{1}{\eta_{diffusion}} + \frac{1}{\eta_{dislocation}}$$

where $\eta_{diffusion}$ and $\eta_{dislocation}$ are viscosities for diffusion and dislocation creep, $\eta_{effective}$ is effective viscosity, P is pressure, T is temperature, $\dot{\varepsilon}_{II} = \sqrt{1/2 \dot{\varepsilon}_{ij} \dot{\varepsilon}_{ij}}$ is the second invariant of the strain rate tensor, σ_{cr} is the diffusion-dislocation creep transition stress, and A_D, E, V, n are strain-rate pre-exponential factor, activation energy, activation volume and stress exponent, respectively. We limit the viscosity to between $1 \times 10^{18} Pas$ and $1 \times 10^{26} Pas$.

A modified version of Drucker-Prager yield criterion (Ranalli, 1995; Byerlee, 1978) is considered for expression of plastic deformation:

$$\tau = C + \phi \lambda_{melt} P \quad (3)$$

where C, λ_{melt} and ϕ are the rock strength at P = 0, melt-induced weakening factor (Gerya et al., 2015) and internal friction coeffi-

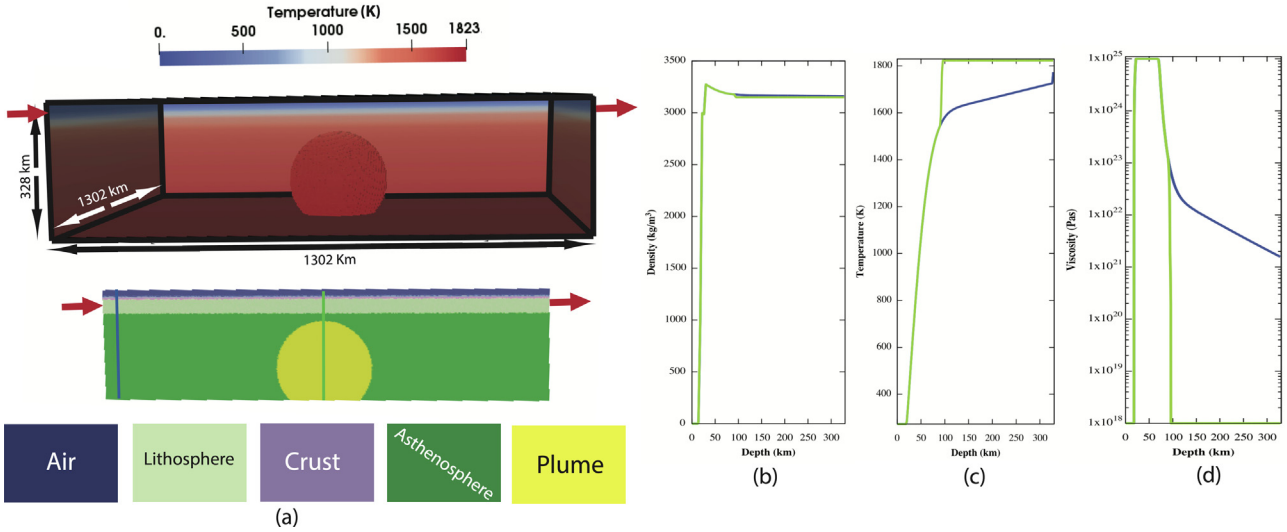

Fig. 1. Initial model setup. (a) Model domain contains oceanic lithosphere, asthenosphere down to 328 km depth and a spherical plume, which develops into a mushroom shape as it rises. The upper panel shows the model temperature field and the lower panel illustrates the compositional field along a cross-section through the middle of the model. Color codes for the compositional field are shown at the bottom of the figure. The red arrows illustrate the imposed velocity boundary condition to simulate plate motion. (b-d) shows the vertical profiles of density, temperature and viscosity along two lines whose locations are shown by green and blue lines in the lower panel of (a). (For interpretation of the references to color in this figure legend, the reader is referred to the web version of this article.)

Table 1
Rheological model parameters. See text for further explanation.

Material	Flow law*	ρ (kg m^{-3})	C (MPa)	φ (–)	A (Pa^n s)	E (KJ mol^{-1})	V (m^3 mol^{-1})	N	K (W m^{-1} K^{-1})	H (μW m^{-3})
Upper crust	Wet quartz	3000	1	0.0	1.97×10^{17}	154	0	2.3	1.18 + 474/(T + 77)	0.25
Lower crust	Plagioclase An75	3000	1	0.2	4.8×10^{22}	238	0	3.2	1.18 + 474/(T + 77)	0.25
Upper and lower crust**	Diabase	3000	1	0.2	1.26×10^{24}	260	0	3.4	1.18 + 474/(T + 77)	0.25
Lithospheric mantle	Dry olivine	3300	1	0.2	3.9×10^{16}	532	0.8×10^{-5}	3.5	0.73 + 1293/(T + 77)	0.022
Asthenosphere	Dry olivine	3300	1	0.2	3.9×10^{16}	532	0.8×10^{-5}	3.5	0.73 + 1293/(T + 77)	0.022
Plume	Wet olivine	3000	1	0.2	5.01×10^{20}	470	0.8×10^{-5}	4	0.73 + 1293/(T + 77)	0.022

* Flow law for all materials are based on (Ranalli, 1995).
** Rheological parameters of the crust in models M31 and M32.

Table 2
List of experiments.

	Age:thickness of oceanic plate (Myr:km)	Plume radius (km)	Plume temperature (K)	Imposed velocity (cm/yr)	Figure name	State of deformation
M1	20:50	140	1820	5	Fig. 2a-d	Single-slab subduction
M2	20:50	140	1820	–	Fig. 2e-h	Multi-slab subduction
M3	40:70	140	1820	5	Fig. 3a-d	Plume penetration without subduction
M4	40:70	140	1820	–	Fig. 3e-h	Plume penetration without subduction
M5	60:85	140	1820	5		Plume penetration without subduction
M6	60:85	140	1820	–		Plume penetration without subduction
M7	20:50	100	1820	5	Fig. 4a-d	No penetration
M8	20:50	100	1820	–	Fig. 4e-h	No penetration
M9	40:70	100	1820	5		No penetration
M10	40:70	100	1820	–		No penetration
M11	60:85	100	1820	5		No penetration
M12	60:85	100	1820	–		No penetration
M13	20:50	170	1820	5		Single-slab subduction
M14	20:50	170	1820	–		Multi-slab subduction
M15	40:70	170	1820	5		Cylindrical subduction
M16	40:70	170	1820	–		Cylindrical subduction
M17	60:85	170	1820	5		Plume penetration without subduction
M18	60:85	170	1820	–		Plume penetration without subduction
M19	20:50	140	1920	5	Fig. 5a-d	Single-slab subduction
M20	20:50	140	1920	–	Fig. 5e-h	Cylindrical subduction
M21	40:70	140	1920	5		Cylindrical subduction
M22	40:70	140	1920	–		Cylindrical subduction
M23	60:85	140	1920	5	Fig. 6a-d	Cylindrical subduction
M24	60:85	140	1920	–	Fig. 6e-h	Cylindrical subduction
M25	20:50	100	1920	5		Penetration without subduction
M26	20:50	100	1920	–		Penetration without subduction
M27	40:70	100	1920	5		No penetration
M28	40:70	100	1920	–		No penetration
M29	60:85	100	1920	5		No penetration
M30	60:85	100	1920	–		No penetration
M31*	20:50	140	1820	5		Single-slab subduction
M32*	20:50	140	1820	–		Multi-slab subduction
M33	20:50	140	1820	10		Single-slab subduction
M34	40:70	140	1820	10		Plume penetration without subduction
M35	60:85	140	1820	10		Plume penetration without subduction

* Rheology of lower oceanic crust in these models are based on Diabase rheology.

cient for the confined fractures, respectively. The internal friction coefficient is calculated as:

$$\phi = \begin{cases} \phi_0\left(1 - \frac{\gamma}{\gamma_0}\right) \text{ for } \gamma \le \gamma_0 \\ 0 \text{ for } \gamma > \gamma_0 \end{cases} \quad (4)$$

and

$$\gamma = \int \sqrt{\dot{\varepsilon}_{ij}^{plastic}\dot{\varepsilon}_{ij}^{plastic}/2}dt \quad (5)$$

where $\gamma \ge 0$ is the time-integrated plastic strain, γ_0 = 0.5 is the upper strain limit for the fracture-related weakening, t is time and $\dot{\varepsilon}_{ij}^{plastic}$ are components of the plastic strain rate tensor. Melt-induced weakening factor is defined as $\lambda_{melt} = 1 - P_{melt}/P$, which depends on the ratio between the melt pressure (P_{melt}) and total pressure (P). Melt-induced weakening is implemented locally within the lithosphere above areas of melt extraction and all other materials have no magmatic weakening ($\lambda_{melt} = 1$). We note that melt-related decrease in the yield strength has been explored not only in the context of plume-oceanic lithosphere interaction (e.g., Ueda et al., 2008; Gerya et al., 2015; Baes et al., 2016; 2020a; 2020b) but also in the case of interaction of plume with continental lithosphere (e.g., Bahadori & Holt, 2019; Koptev et al., 2021; Beniest et al., 2017a; 2017b).

The friction coefficient of all model layers is 0.2 except in the upper crust, which has zero friction coefficient to lubricate the plate interface when the lithosphere subducts.

Melt extraction and melt percolation are defined in a simplified manner (see Gerya, 2013; Gerya et al., 2015). In this method the total amount of melt for Lagrangian markers, which are used to track the melt extraction, is calculated as:

$$M = M_0 - \sum_m M_{ext} \quad (4)$$

where M_0 and $\sum_m M_{ext}$ are the standard volumetric degree of mantle melting and total melt fraction extracted during the previous melt extraction episodes. Slab dehydration and mantle hydration is based on the water markers approach (Gerya and Meilick, 2011) in which the equilibrium mineralogical water content for the crust and the mantle is defined as a function of pressure and temperature from thermodynamic data by free energy minimization. Eclogitization is expressed by a linear increase of density with pressure from 0% to 16% in the PT-region between the garnet-in and plagioclase-out phase transitions in basalt (Ito and Kennedy, 1971).

The initial temperature field of the oceanic lithosphere is calculated on the basis of cooling half-space formulation (Turcotte and Schubert, 1982). The temperature in the asthenosphere is adiabatic with a gradient of ~ 0.5 K km^{-1}. Temperature of the plume is 1820 K, which is 200 K hotter than ambient mantle. In some models we increase the plume temperature to 1920 K to evaluate the effect of plume temperature on the results (Table 2). Temperature within the sticky air is constant (273 K). The upper boundary of the model has an initial thermal boundary condition of 273 K. The boundary conditions across the vertical model sides are zero horizontal heat flux. An infinity-like external temperature condition (Gerya, 2010) is imposed on the lower boundary.

The moving plate is simulated by imposing a kinematic boundary condition (5 cm/yr) on the lithospheric part of the left and right boundaries. We consider free slip boundary conditions for the right and left mode sides below the lithosphere and all other boundaries, except the bottom of the model, which is an open permeable boundary.

Table 2 describes the experiments we performed in this study. The experiments differ in the age of the lithosphere, existence or absence of plate motion and size and temperature of the mantle plume. To analyze the effects of lithospheric age, we carried out experiments with lithospheric ages of 20, 40 and 60 Myr. The effect of plume buoyancy is investigated by considering plumes with radiuses of 100, 140 and 170 km and temperatures of 1820 and 1920 K in various experiments.

2.2. Model results

2.2.1. Reference model

Model M1, representing the reference model, is characterized by an initial plume head radius of 140 km, lithospheric age of 20 Myr and plume temperature of 1820 K (Table 2). To better acknowledge the effect of plate motion in Fig. 2 we show the results of reference model together with those of similar experiment but without plate motion (model M2 in Table 2). Results of model M1 demonstrate that at 0.036 Myr after model start, the

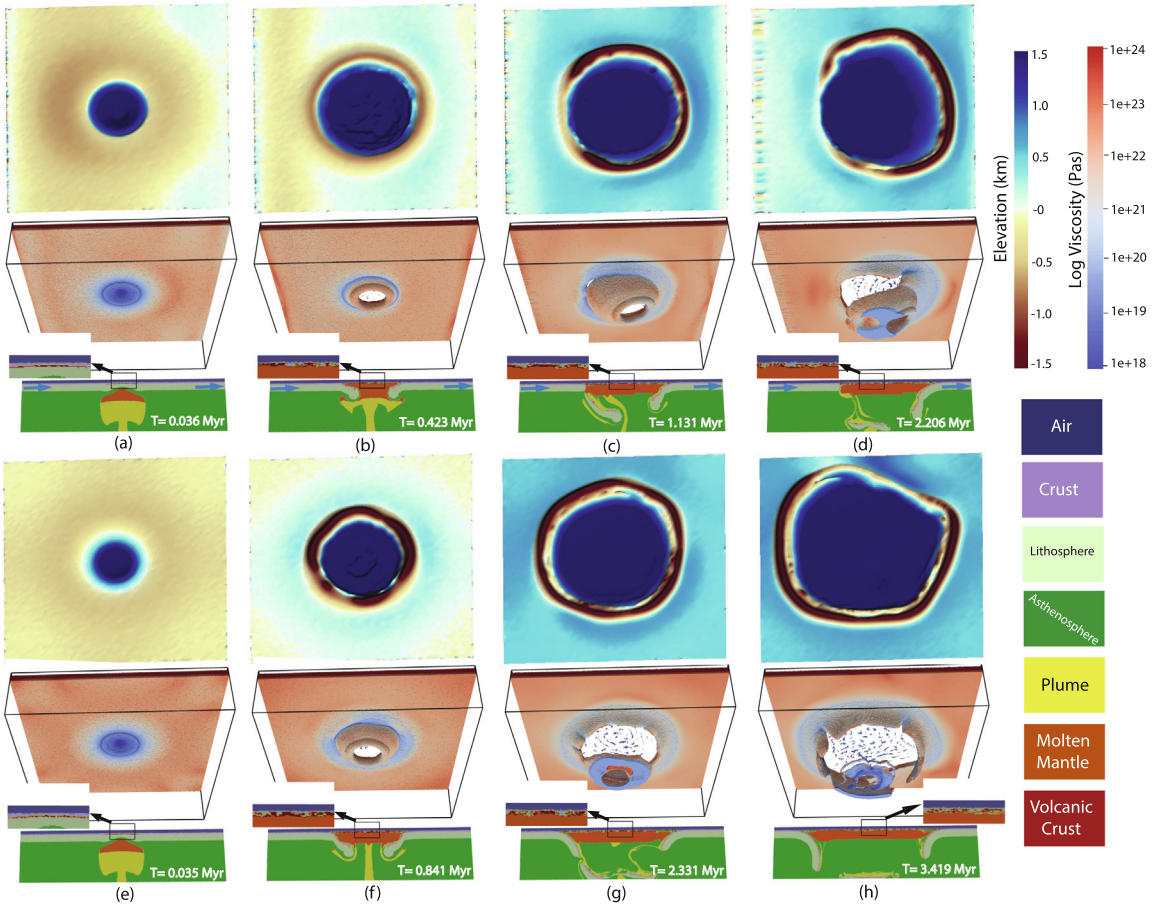

Fig. 2. Results showing the influence of plate motion on plume-lithosphere interaction. Outcomes of: (a-d) reference model (M1) where the lithosphere is moving (from the left to the right) relative to the asthenosphere at 5 cm/yr and (e-h) model M2 which is similar to the reference model but without moving lithosphere. The upper, middle and lower panels stand for surface topography (top view), viscosity field of lithosphere and compositional field (color codes as shown on the bottom-right side of figure) of a 2d cross-section through the model center, respectively. Insets show a zoom in of the uppermost lithosphere above the plume head. Blue arrows in lower panels of (a-d) indicate the direction of plate motion. Comparing results of model M1 and M2 indicates that interaction of a plume with young lithosphere can lead to subduction initiation. In this case, plate motion causes formation of a single-slab subduction (instead of multi-slab subduction). See detailed evolution of models M1 and M2 in Supplementary videos V1 and V2. (For interpretation of the references to color in this figure legend, the reader is referred to the web version of this article.)

mushroom-shaped plume penetrates the lower lithosphere (Fig. 2a). This is coeval with melting of the upper plume head (light red-colored area in lower panel of Fig. 2a), resulting in formation of volcanic-plutonic crust (dark red area in inset of lower panel of Fig. 2a) and weakening of the overlaying lithosphere. A circular uplifted dome-shaped region forms at the surface above the plume head (Fig. 2a upper panel). A plateau forms above the plume head as a result of development of volcanic-plutonic crust. With time, the plume breaks the lithosphere and spreads above broken segments of the lithosphere pushing them downwards (Fig. 2b). Due to further melt extraction and rising of more plume material, the circular shaped plateau broadens and its thickness (inset of lower panel in Fig. 2b) increases. As a result, the uplifted area in the model center widens (upper panel of Fig. 2b). Later, due to eastward motion of lithosphere, the proto-slab on the left model side encounters the plume tail causing deviation of flow direction. Flowing of more mantle plume towards the left causes breaking off the slab from the left side thereby causing transition to single-slab subduction (Fig. 2c-d) that is more comparable to modern-style plate tectonics (Baes et al., 2020a). A surface depression develops on the right side of the circular dome, representing development of a trench (upper panel of Fig. 2c). After slab break-off from the left side, subduction continues from the other side; the surface depression deepens and trench rollback causes widening of the uplifted plateau region (Fig. 2d).

The initial deformation regime of model M2 is similar to that of the reference model (comparing Fig. 2a and Fig. 2e). A circular plateau forms above the plume head as a result of partial melting of plume rocks (Fig. 2e). With time, the deformation deviates from that in the reference model illustrating the effect of the absence of plate motion on plume-lithosphere interaction (compare Fig. 2-b-d and Fig. 2f-h). A symmetrical (cylindrical) slab forms and sinks further into the mantle with time (Fig. 2f). Consequently, a circular-shaped depression develops on the surface (upper panel of Fig. 2f). Uprising of plume rocks above proto-slabs induces thinning of the slab segments. This leads to heating of the slab and eventually its partial break-off and subsequent multiple tearing (Fig. 2g-h). This process leads to development of a pronounced multi-slab subduction (Fig. 2h) notably contrasting with the single-slab subduction obtained in the reference model with the moving plate (cf. Fig. 2d and h).

2.2.2. Effect of lithospheric age

Fig. 3a-d shows the temporal evolution of model M3 which has a same setup as the reference model M1 except that the lithosphere is older (40 Myr – Table 2). Similar to the reference model, as the plume rises and encounters the bottom of lithosphere, the surface is uplifted in a circular region above the plume head (upper panel of Fig. 3a). Melt extraction from plume head rocks and their migration towards the surface forms a plateau. Later, the plume penetrates the lithosphere creating a circular hole (Fig. 3b). Plateau thickness increases as a result of more melt extraction and production of plutonic-volcanic rocks (inset in lower panel of Fig. 3b). Consequently, the surface topography is further elevated above the plume head (upper panel of Fig. 3b). Due to plate motion, the plateau created by plume-lithosphere interaction moves right

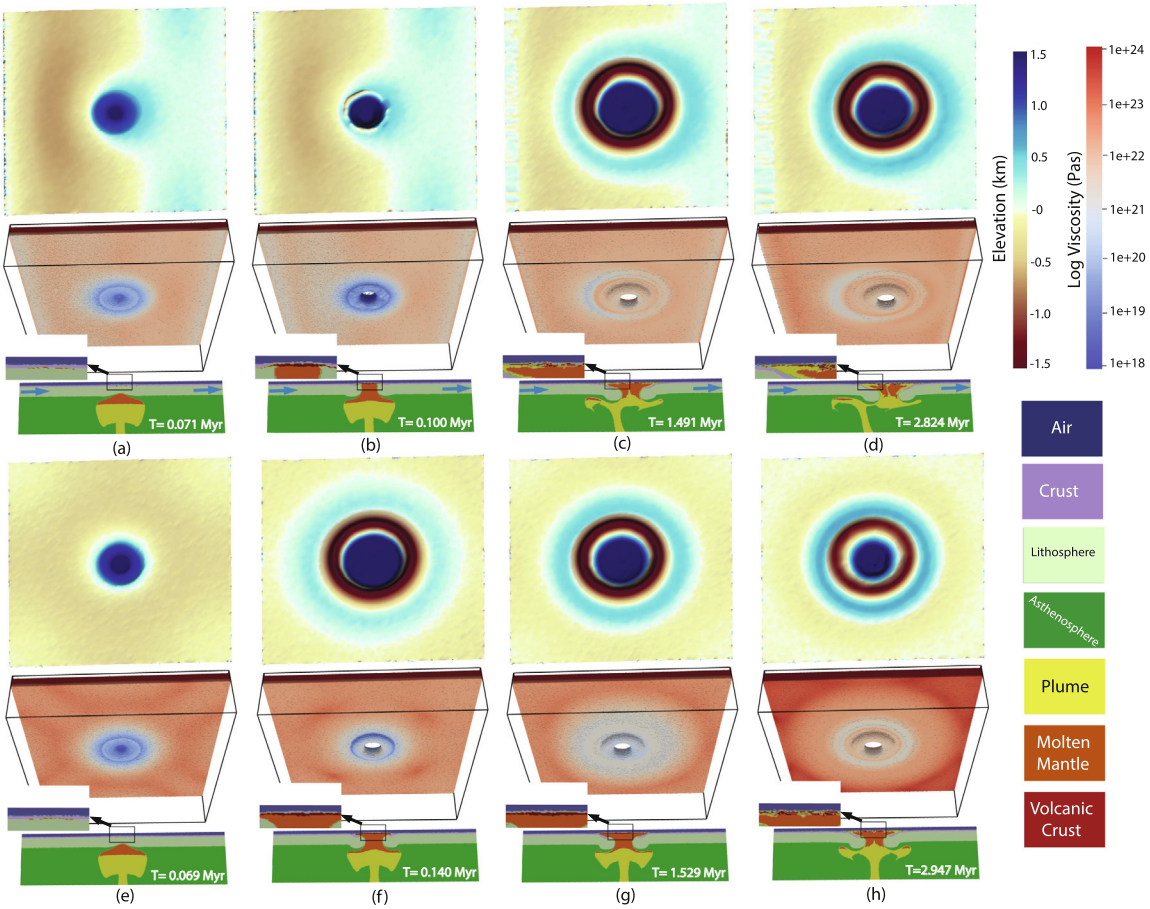

Fig. 3. Effect of lithospheric age: (a-d) Model M3 is similar to reference model M1 but with older lithosphere (40 Myr instead of 20 Myr). (e-h) Model M4 is identical to M3 but without plate motion. For explanation of panel meanings, see Fig. 2 caption. This figure shows that due to aging (and hence the strength) of the lithosphere plume-lithosphere interaction can lead to penetration without subduction initiation. In this case, plate motion has a minor effect on deformation caused by impingement of a mantle plume with the overriding lithosphere.

(Fig. 3c). Lava flows increase elevation and broaden the uplifted area. Spreading of plume rocks atop broken segments of lithosphere forces the oceanic plate to bend down (Fig. 3c). This produces subsidence around the uplifted region. The lithosphere cannot sink deeper due to its strength and resistance to further bending. As the plateau moves right, away from the plume, melting decreases (Fig. 3d); consequently, uplifted areas subside. A similar model but without plate motion (model M4 in Table 2) shows comparable results (Fig. 3e-h) except that here (a) the motion of the plateau created by plume- lithosphere interaction is absent, and (b) the lowermost lithosphere is more viscous compared to that in model M3 as a result of shear stresses associated with lithospheric motion.

2.2.3. Effect of plume size

One of the parameters controlling plume buoyancy is its size. Outcomes of model M7, in which we decrease the size of plume to 100 km, indicate that the plume does not penetrate the lithosphere (Fig. 4a). In comparison to the reference model, the plateau, which forms above the plume head, is thinner due to less melt production and melt extraction. As a result, the elevation of the uplifted area is considerably lower than that in the reference model. Since the plume cannot penetrate the lithosphere it spreads symmetrically beneath it in the initial stages of plume-lithosphere interaction. This leads to an increase in the size of the plateau and hence the uplifted surface area (Fig. 4b). Later, plate motion causes asymmetric underplating of the plume and its propagation towards the right side of model (Fig. 4c-d). Consequently, the uplifted surface area changes its shape from circular to ellipsoidal. We note that the elapsed model time (2.85 Myr) is too short to develop a clearly elongated topographic chain (such as the Hawaiian chain).

Results of model M8 are shown in Fig. 4e-h. This model is similar to M7 except that here the lithosphere is stationary. The deformation regime is similar to that of model M7 indicating no plume penetration. Due to the stationary plate, the spreading of the plume beneath the lithosphere continues symmetrically. This is coeval with preservation of the circular shape of the uplifted plateau above the plume head. In addition, the viscosity of the bottom of the lithosphere is higher than that in model M7 as a result of low shear stress accumulation between the lithosphere and the underlying asthenosphere.

2.2.4. Effect of plume temperature

Previous studies indicate that plume excess temperature in the upper mantle varies between 200 and 300 K (e.g., Schilling, 1991; Herzberg and Gazel, 2009). The excess temperature of the plume with respect to ambient mantle in the reference model is 200 K. In models M19-30 we increase the thermal buoyancy of the plume by considering a hotter mantle plume (100 K hotter than model M1). Results of model M19, which is similar to the reference model but has a hotter plume, are shown in Fig. 5a-d. When the plume rises, considerable portions of the plume head melt (Fig. 5a). The amount of melt production and melt extraction are significantly higher than in the reference model; therefore, the plateau is thicker. The plume head breaks the lithosphere and overrides the

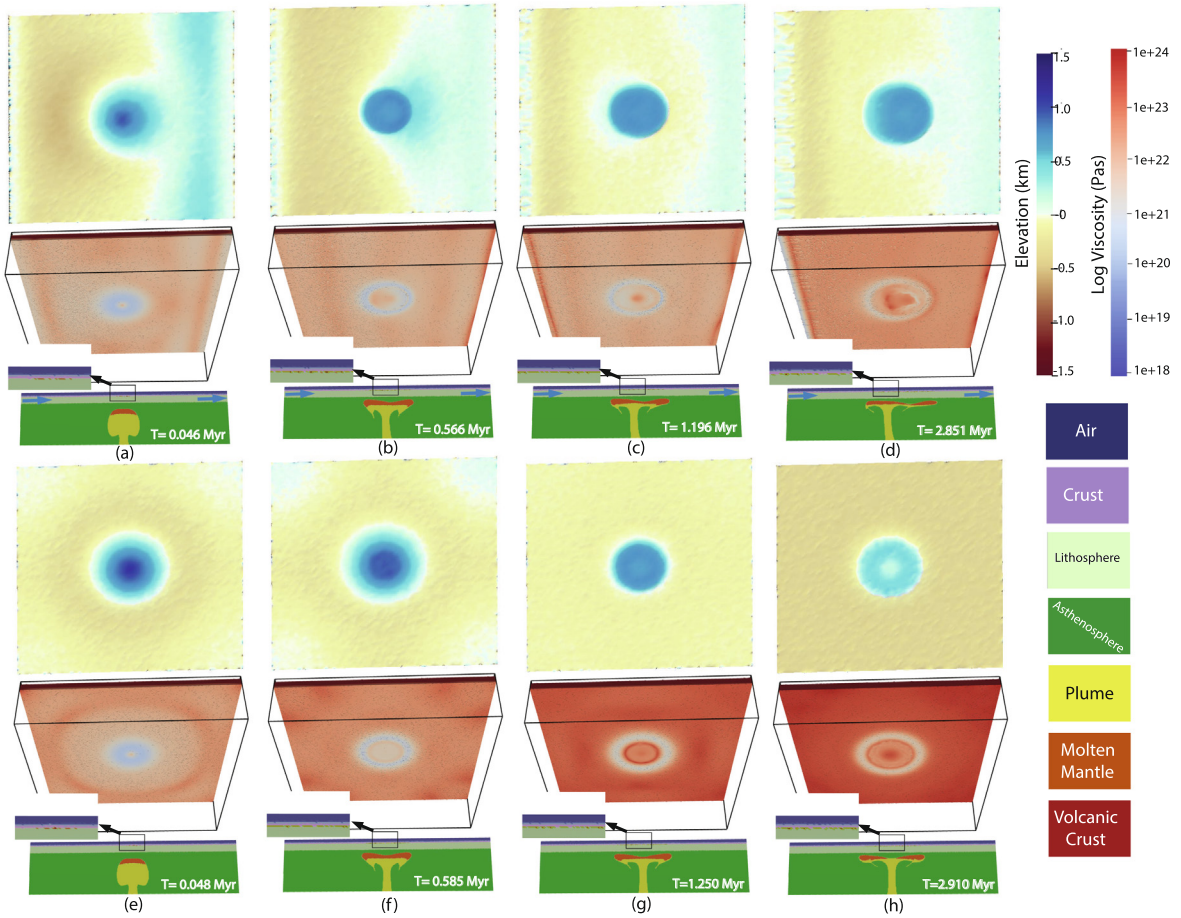

Fig. 4. Effect of plume size: (a-d) Model M7 is identical to the reference model M1 except that the plume is smaller (with radius of 100 km instead of 140 km). (e-h) M8 differs from model M7 by excluding plate motion. For explanation of panels, see Fig. 2 caption. Results of models M7 and M8 show that a small plume head cannot break the lithosphere and the effect of plate motion in this case is minor.

broken lithosphere, creating a cylindrical slab (Fig. 5b). The plateau extends due to the rolling back of the slab and continuous melt extraction (inset in lower panel of Fig. 5b). A ring-shaped subsidence region forms around the plateau marking the trench location. Due to plate motion towards right, the slab on the right side breaks off (Fig. 5c-d), creating an asymmetric single-slab subduction, however with polarity that is opposite to the reference model (cf. Fig. 2c,d and 5c,d). The direct effect of slab break-off on the surface topography is the reduction of subsidence (i.e. uplift) on the right side of the ring-shape trench (upper panel of Fig. 5c). Subduction on the left model side continues to sink into the mantle (Fig. 5d). A similar experiment but without plate motion (model M20 in Table 2) indicates that the plume breaks the lithosphere and the proto-slabs sink into the mantle (Fig. 5e-f). In the case of stationary plate, the plume spreads symmetrically, resulting in development of a uniform cylindrical subduction (Fig. 5g). Later, the slab breaks off totally indicating termination of subduction (Fig. 5h).

Fig. 6a-d illustrates the results of model M23 which differs from the reference model in having a 100 K hotter plume and 40 Myr older oceanic lithosphere. After plume penetration (Fig. 6a) and development of a subducting slab, due to the plate motion the slab tip on the left side encounters the plume tail leading to deflection of plume flow towards the left (Fig. 6b). This thins the slab on the left side of the model creating notable asymmetry of the cylindrical slab (Fig. 6b). Later, subduction of the asymmetric, partially broken cylindrical slab continues without slab break-off (Fig. 6c-d). This indicates that in contrast to the reference model, here the stresses arising from plate motion are not sufficient to overcome the strength of the old slab and cause its tearing and transition to a single-slab subduction regime (cf. Fig. 2c-d and 6c-d). Slab rollback leads to increasing plateau size and trench lengthening (Fig. 6c-d). A similar experiment but without plate motion (model M24 in Table 2) demonstrates that when a plume hits old stationary lithosphere it breaks the plate and spreading of plume materials symmetrically above the broken lithosphere leads to development of a uniform symmetrical cylindrical slab (Fig. 6e-h). In this case due to stationary plate and trench retreat, slab never encounters with plume tail and consequently the thickness of slab is uniform.

3. Discussion

Plate motion, which reflects the interaction of the lithosphere with the asthenosphere, is a key component in geosciences. In this study, we investigate the influence of plate motion on plume-lithosphere interaction including the effect of melt weakening. Numerical results show that the impact of plate motion becomes noticeable when a sufficiently buoyant plume (with plume head radius of 140 km or bigger) encounters oceanic lithosphere (Fig. 7 and Table 2). Regardless of plume temperature and plate motion, small plumes either do not penetrate the lithosphere (red circles in Fig. 7) or create small plateaus (illustrated by brown circles as penetration without subduction initiation in Fig. 7). Larger and hotter plumes facilitate subduction initiation (Fig. 7 and

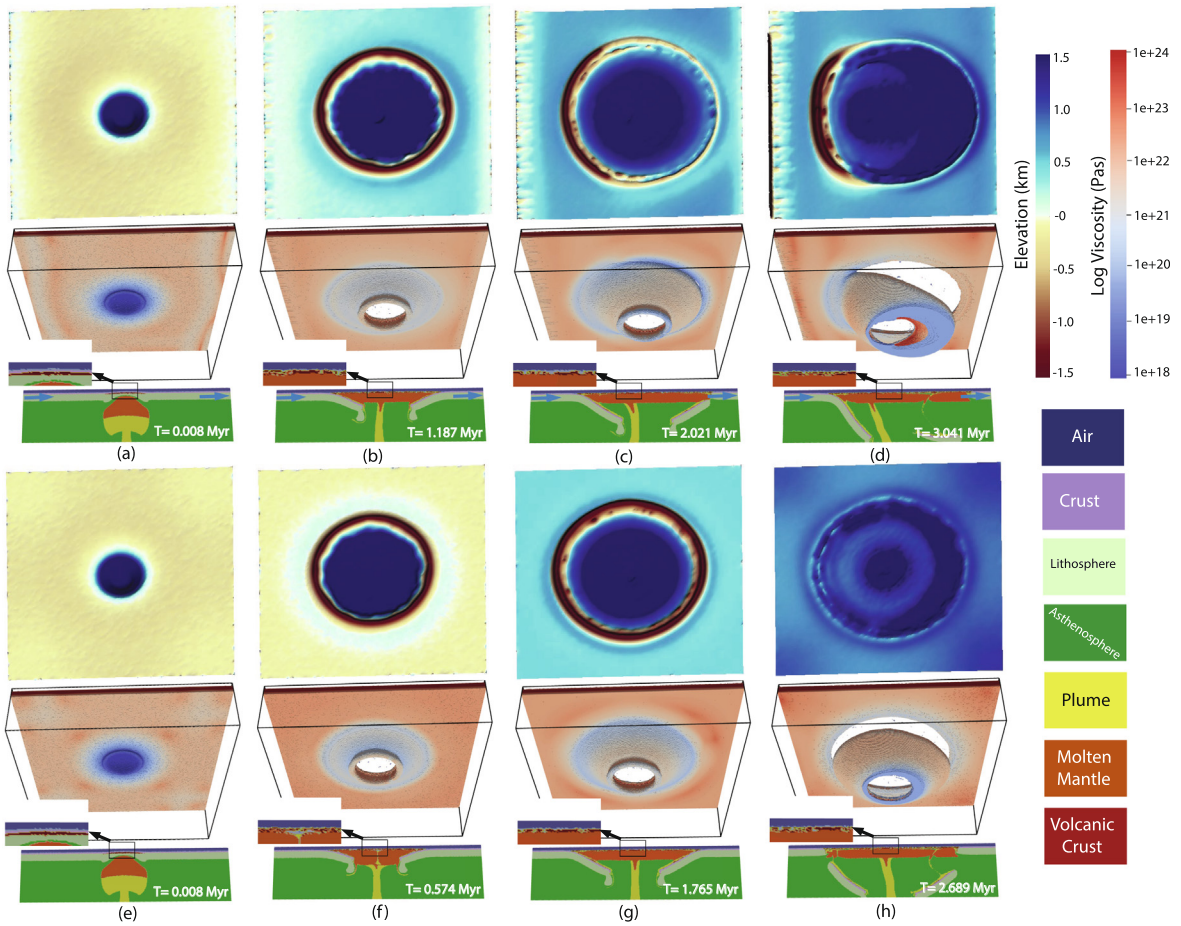

Fig. 5. Effect of plume temperature: (a-d) Model M19 differs from reference model M1 in having a hotter plume (T = 1920 K). (e-h) Model M20 is similar to model M19 but without plate motion. For explanation of panels, see Fig. 2 caption. Figure illustrates that asymmetric flow caused by plate motion can lead to initiation of single-slab subduction. See detailed evolution of models M19 and M20 in Supplementary videos V3 and V4.

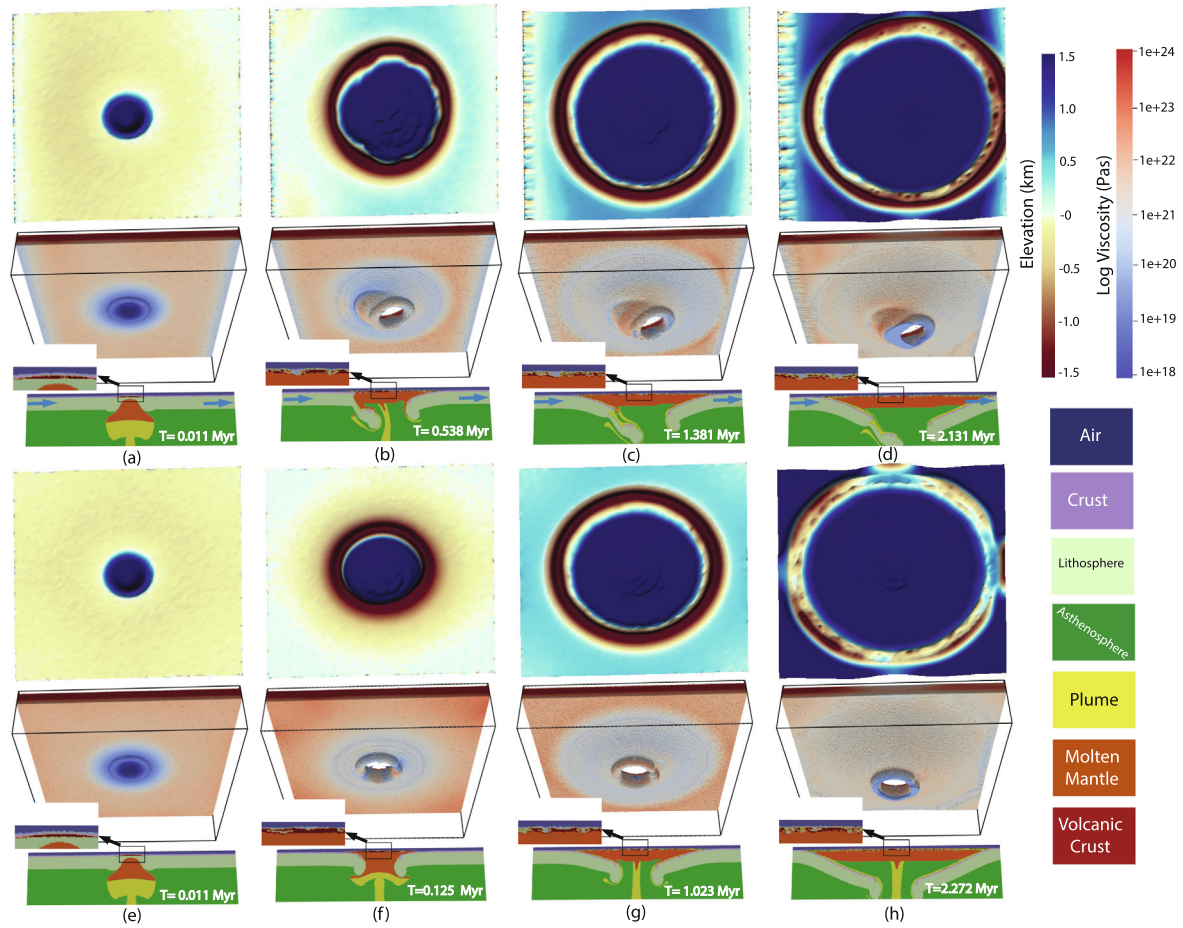

Fig. 6. Effect of plume temperature and lithospheric age: (a-d) Model M23 differs from reference model M1 in having a hotter plume (with temperature of 1920 K) and older oceanic lithosphere (60 Myr). (e-h) Model M24 is similar to model M23 but without plate motion. For explanation of panels, see Fig. 2 caption. Figure illustrates that the interaction of a hot mantle plume with an old moving oceanic lithosphere may results in local thinning of subducting slab. Detailed evolution of models M23 and M24 are shown in Supplementary videos V5 and V6.

Table 2). This agrees with previous studies indicating the key role of plume buoyancy on subduction initiation (Ueda et al., 2008, Gerya et al., 2015; Baes et al, 2016; 2020a; 2020b). In this study, we have shown that when a mantle plume with a radius of 140 km or bigger arrives beneath 20-Myr old oceanic lithosphere, the resulting deformation clearly depends on plate motion. Asymmetrical single-slab subduction is promoted in experiments with moving plates (Fig. 2a-d, 5a-d and 7 and Table 2). In these models, slab break-off occurs due to either the interplay of the young (and hence weak) subducting slab with the plume tail (Fig. 2a-d) or higher plume flow in the direction of motion (Fig. 5a-d). The polarity of the resultant subducted slab depends on the buoyancy of the plume which controls the rate of trench retreat. In the reference model (Fig. 2a-d) due to lower trench retreat compared to model M19 (Fig. 5a-d), newly formed slab interacts with the plume tail, deflecting the plume flow towards the left. This flow causes slab break-off from the left. However, in the case of model M19 with hotter plume, due to higher trench retreat and eastward (to the model right) plate motion, the distance between the slab on the right model side and plume tail increases with time. Higher trench retreat causes upward motion of more asthenospheric material on the right side which finally weakens and breaks the slab from that side. In the case of a hotter mantle plume interacting with an older oceanic plate, the asymmetry of the subducting cylindrical slab persists in models with plate motion (Fig. 6a-d). In contrast, in the absence of plate motion, more symmetrical multi-slab (e.g., Fig. 2e-h) or symmetric circular subduction (Fig. 5e-h, 6e-h) regimes dominate.

When the lithosphere is strong, the forces induced by the mantle plume may not be large enough to overcome lithospheric strength. As a result, the plume spreads beneath the lithosphere without rupturing it (red circles in Fig. 7). Larger and hotter plume heads lead to more magmatic weakening, which can lead to plume penetration. Plume penetration and lithospheric rupture may result in subduction initiation if the flexural resistance of the lithosphere is overcome by its negative buoyancy and extra gravitational force coming from overriding of the plume head rocks over the broken lithosphere (green circles in Fig. 7). In this case, due to high lithospheric strength, the interaction of subducting lithosphere with the plume tail may thin the slab but not cause slab break-off and/or tearing (see Fig. 6a-d). If plume buoyancy is insufficient, the deformation regime remains as plume penetration without subduction initiation (brown circles in Fig. 7). Th summary of our results (Fig. 7 and Table 2) demonstrates that the critical plume head radius needed to break the lithosphere depends on plume buoyancy and lithospheric age, but not on plate speed. This is because the rate of melt extraction which causes lithospheric magmatic weakening is higher than the rate of plate motion.

Lithospheric response to arrival of a mantle plume beneath it depends on several parameters including lithospheric strength, plate motion and plume buoyancy (Table 2 and Fig. 7). As indicated by previous studies, other tectonic events such as extension, com-

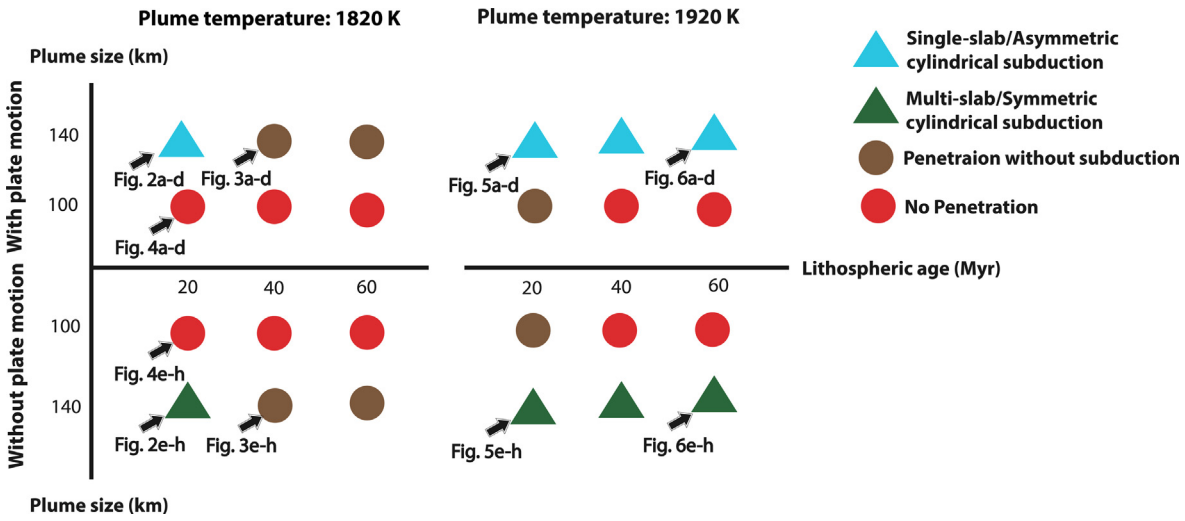

Fig. 7. Summary of model results. The horizontal and vertical axes indicate lithospheric age and inclusion (positive direction) or exclusion (negative direction) of plate motion. Results of models with plume temperatures of 1820 K and 1920 K are shown on the left and right side of horizontal axis, respectively. The corresponding figures for those models illustrated in Figs. 2–6 are indicated below the respective circles.

pression, pre-existing weakness zones in the lithosphere (e.g., Baes et al, 2016) and crustal or lithospheric heterogeneities (Baes et al., 2020a; 2020b) may affect the deformation regime.

Arrival of a plume beneath the lithosphere generates a plateau (Figs. 2-6) that thickens and broadens with time. The rate of plateau growth in size and thickness differs in experiments with different deformation regimes. In the case of PISI, a thick plateau forms and broadens with time due to high melt extraction and slab rollback (Fig. 2,5 and 6). Plateaus are smaller if there is no penetration or penetration without subduction initiation (Figs. 3-4). Thickness of plateaus increases with increasing plume buoyancy. In our experiments, plateau thickness varies between ~10 and ~20 km in different models.

Plume underplating (we call it no penetration) is common for the modern Earth. Natural examples of plume spreading beneath the lithosphere are associated with various Large Igneous Provinces (LIPs), such as Siberia (Gerald et al., 1998; Sobolev et al., 2011), Tarim (Long et al., 2011; Wie et al., 2014) and Hawaii (Li et al., 2004; Bono et al., 2019). This lithospheric response to plume-lithosphere interaction occurs if plume buoyancy is insufficient to overcome lithospheric strength (e.g., model M7 in Fig. 4). As a result, the plume flattens below the lithosphere and partially melts, creating a plateau. The surface topography indicates that the initial uplift (blue curves in Fig. 8), which is due to rising mantle plume head and the subsequent subsidence (red, yellow and purple curves in Fig. 8) induced by flattening of the plume head, depend on the age (strength) of the lithosphere and plate motion. Initial uplift (blue curves in Fig. 8) is greater for younger plates due to the low flexural resistance. A surface depression develops above the plume head (Fig. 8) as a consequence of weakening the lithosphere by the plume head, which causes Rayleigh-Taylor-like instability. The depth of this depression decreases with increasing lithospheric strength (Fig. 8). These results are consistent with those of Burov and Guillou-Frottier (2005) and Brune et al. (2013) who showed that plumes may generate alternating small-scale surface topography. Fig. 8 demonstrates that the main influence of plate motion on surface topography is (a) formation of asymmetric topography and (b) increasing of width of the uplifted area (Fig. 8).

The first evidence of plume-induced subduction initiation at the southern and western margins of the Caribbean Plate (Whattam and Stern 2014) made a big step towards understanding the important role that mantle plumes played in starting some subduction zones. The open question regarding numerical models and observations is: which factors were the controlling parameters for forming single-slab (instead of multi-slab) subduction around the Caribbean region? Different reasons have been suggested including pre-existing compositional and density contrasts between the 140–110 Ma plateau and normal oceanic lithosphere (Whattam and Stern, 2014), plume-plateau interaction in an extensional regime or interaction of plume with a normal oceanic crust (Baes et al., 2020a) and plume impingement close to the plateau-oceanic crust transition (Baes et al., 2020b). Our study reveals that plate motion is also important for single-slab subduction initiation. We propose that new subduction zones formed around the western and southern Caribbean plate due to the arrival of a sufficiently buoyant plume below a young but subductable lithosphere (20 Myr in our experiments). The eastward motion of Farallon plate at the time of plume-lithosphere interaction (~100 Ma) could have resulted in slab break off on the east and continuation of subduction in the west (similar to that shown in Fig. 5a-d). Petrologic studies showed that the Caribbean plume was hottest during the early head melting stage (>1700 °C (Herzberg and Gazel, 2009; Trela et al., 2017)). Whittaker et al., (2015) noted that Caribbean plateau formed on oceanic lithosphere older than 10 Myr. These observations are agree with results of model M19 (Fig. 5a-d) in which a hot mantle plume interacts with 20-Myr-old oceanic lithosphere and results in single-slab subduction initiation. Plateau thickness in this model is ~20 km which matches well with the estimated thickness of the Caribbean plateau (Sinton et al., 1998; Revillon et al., 2000).

4. Conclusions

We have shown that plate motion affects plume head-lithosphere interactions by promoting asymmetry of subduction zones. When a sufficiently buoyant plume head hits a young but subductable lithosphere, interaction of a newly-formed subducted slab with the plume in the direction of plate motion causes asymmetric deformation, breaking off the slab from the leading edge and favoring single-slab subduction. In the case of subduction initiation induced by interaction of a mantle plume head with older oceanic lithosphere, the greater strength of this lithosphere and interaction of the slab with the plume tail may lead to localized thinning instead of slab break-off, producing asymmetric cylindri-

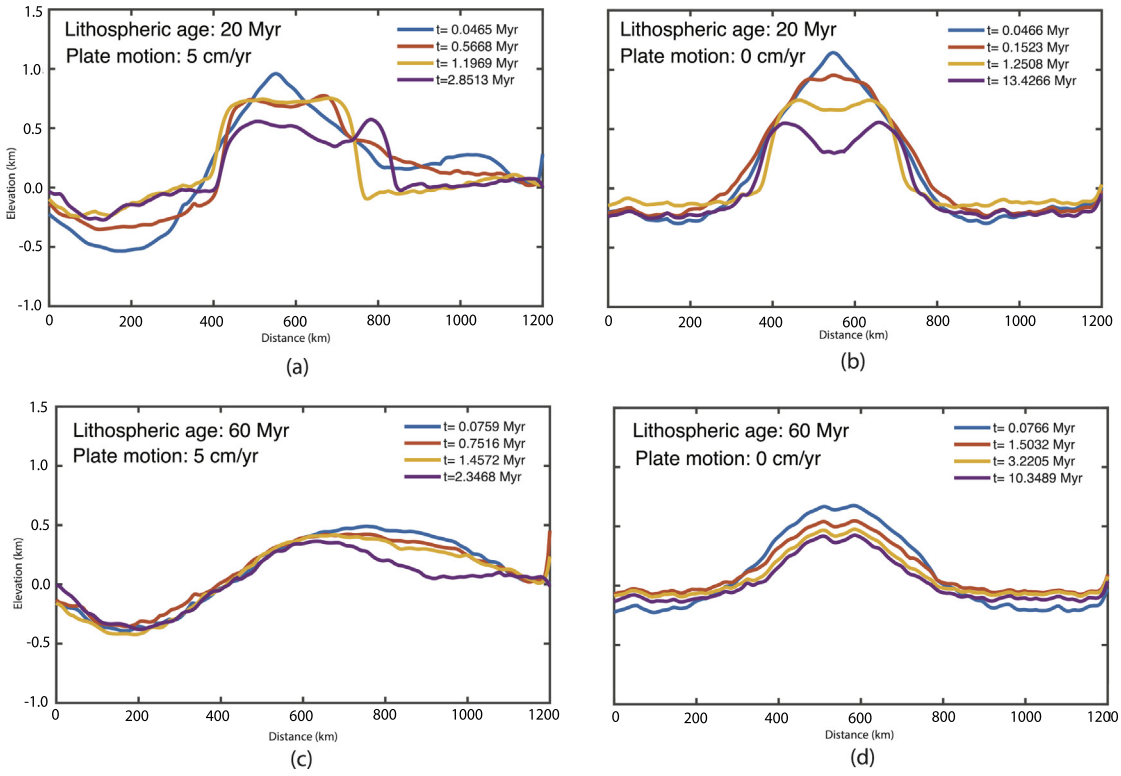

Fig. 8. Temporal evolution of surface topography for models involving plume underplating: (a) M7 which is similar to reference model but with smaller plume size (radius = 100 km), (b) M8 which differs from model M7 by excluding plate motion, (c) M11 which is similar to M7 but with a lithospheric age of 60 Myr, and (d) M12 which is like model M11 but without plate motion.

cal subduction. Different combinations of various model parameters show that the arrival of a plume head beneath the lithosphere can either (1) break the lithosphere and initiate subduction, (2) penetrate the lithosphere without subduction initiation, or (3) spread asymmetrically below the lithosphere. Outcomes indicate that lithospheric strength and plume buoyancy are key parameters in penetration of plume and that the plate speed has a negligible effect. Surface topography evolution illustrates that due to the plate motion, the size of the new plateau increases in the direction of plate movement. Our results indicate that motion of the Farallon plate to the NE was an important reason why new subduction zones formed on the southern and western margins of the Caribbean Plate at ~100 Ma.

CRediT authorship contribution statement

Marzieh Baes: Conceptualization, Methodology, Validation, Investigation, Writing - original draft, Visualization. **Stephan Sobolev:** Validation, Writing - review & editing. **Taras Gerya:** Conceptualization, Validation, Software, Writing - review & editing. **Robert Stern:** Conceptualization, Validation, Writing - review & editing. **Sascha Brune:** Validation, Writing - review & editing, Funding acquisition.

Declaration of Competing Interest

The authors declare that they have no known competing financial interests or personal relationships that could have appeared to influence the work reported in this paper.

Acknowledgments

This study has been funded by the German Science Foundation (DFG) (Projects BR 5815/1-1 and BA 6613/2-1). The computations of this work was supported by the North-German Supercomputing Alliance (HLRN). We thank Zhong-Hai Li and Alexander Koptev for their careful reading of the manuscript and their constructive remarks.

Appendix A. Supplementary material

Supplementary data to this article can be found online at https://doi.org/10.1016/j.gr.2021.06.007.

References

Baes, M., Govers, R., Wortel, R., 2011a. Subduction initiation along the inherited weakness zone at the edge of a slab: Insights from numerical models. Geophys. J. Int. 184, 991–1008. https://doi.org/10.1111/j.1365-246X.2010.04896.x.

Baes, M., Govers, R., Wortel, R., 2011b. Switching between alternative responses of the lithosphere to continental collision. Geophys. J. Int. 187, 1151–1174. https://doi.org/10.1111/j.1365-246X.2011.05236.x.

Baes, M., Gerya, T.V., Sobolev, S.V., 2016. 3-D thermo-mechanical modeling of plume-induced subduction initiation. Earth Planet. Sci. Lett. 453, 193–203.

Baes, M., Sobolev, S.V., 2017. Mantle flow as a trigger for subduction initiation: a missing element of the Wilson Cycle concept. Geochem. Geophys. Geosyst. 18, 4469–4486.

Baes, M., Sobolev, S.V., Quinteros, J., 2018. Subduction initiation in mid-ocean induced by mantle suction flow. Geophys. J. Int. 215, 1515–1522.

Baes, M., Sobolev, S.V., Gerya, T.V., Brune, S., 2020a. Plume-induced subduction initiation: Single-slab or multi-slab subduction? Geochem. Geophys. Geosyst. 21, e2019GC008663.

Baes, M., Sobolev, S.V., Gerya, T.V., Brune, S., 2020b. Subduction initiation by plume-plateau interaction: Insights from numerical models. Geochem. Geophys. Geosyst. 21, e2020GC009119.

Bahadori, A., Holt, W.E., 2019. Geodynamic evolution of southwestern North America since the Late Eocene. Nature Commun. 10, 521. https://doi.org/10.1038/s41467-019-12950-8.

Beniest, A., Koptev, A., Leroy, S., Sassi, W., Guichet, X., 2017a. Two-branch break-up systems by a single mantle plume: Insights from numerical modeling. Geophys. Res. Lett. 44, 9589–9597.
Beniest, A., Koptev, A., Burov, E., 2017b. Numerical models for continental break-up: implications for the South Atlantic. Earth Planet. Sci. Lett. 461, 176–189.
Bono, R.K., Tarduno, J.A., Bunge, H.P., 2019. Hotspot motion caused the Hawaiian-Emperor Bend and LLSVPs are not fixed. Nat. Commun. 10, 3370. https://doi.org/10.1038/s41467-019-11314-6.
Boschman, L.M., van der Wiel, E., Flores, K.E., Langereis, C.G., van Hinsbergen, D.J.J., 2019. The Caribbean and Farallon plates connected: constraints from stratigraphy and paleomagnetism of the Nicoya Peninsula, Costa Rica. J. Geophys. Res. 124, 6243–6266. https://doi.org/10.1029/2018JB016369.
Brune, S., Popov, A.A., Sobolev, S.V., 2013. Quantifying the thermo-mechanical impact of plume arrival on continental break-up. Tectonophysics 604, 51–59. https://doi.org/10.1016/j.tecto.2013.02.009.
Burov, E., Cloetingh, S., 2009. Controls of mantle plumes and lithospheric folding on modes of intra-plate continental tectonics: differences and similarities. Geophys. J. Int. 178, 1691–1722.
Burov, E., Cloetingh, S., 2010. Plume-like upper mantle instabilities drive subduction initiation. Geophys. Res. Lett. 37, L03309. https://doi.org/10.1029/2009GL041535.
Burov, E., Guillou-Frottier, L., 2005. The plume head–continental lithosphere interaction using a tectonically realistic formulation for the lithosphere. Geophys. J. Int. 161, 469–490. https://doi.org/10.1111/j.1365-246X.2005.02588.x.
Byerlee, J., 1978. Friction of rocks. Pure Appl. Geophys. 116, 615–626.
Cloetingh, S.A.P.L., Wortel, M.J.R., Vlaar, N.J., 1982. Evolution of passive continental margins and initiation of subduction zones. Nature 297, 139–142.
Cloetingh, S.A.P.L., Wortel, M.J.R., Vlaar, N.J., 1984. Passive margin evolution, initiation of subduction and the Wilson cycle. Tectonophysics 109, 147–163.
Cloetingh, S.A.P.L., Wortel, M.J.R., Vlaar, N.J., 1989. On the initiation of subduction zones. Pure Appl. Geophys. 129, 7–25.
Cloetingh, S., Koptev, A., Kovács, I., Gerya, T., Beniest, A., Willingshofer, E., et al., 2021. Plume-induced sinking of intra-continental lithospheric mantle: An overlooked mechanism of subduction initiation? Geochem. Geophys. Geosyst. 22, e2020GC009482.
Crameri, F., Tackley, P.J., 2016. Subduction initiation from a stagnant lid and global overturn: new insights from numerical models with a free surface. Prog. Earth Planet. Sci. 3, 30. https://doi.org/10.1186/s40645-016-0103-8.
Crameri, F., Schmeling, H., Golabek, G.J., Duretz, T., Orendt, R., Buiter, S.J.H., et al., 2012. A comparison of numerical surface topography calculations in geodynamic modelling: an evaluation of the 'sticky air' method. Geophys. J. Int. 189, 38–54. https://doi.org/10.1111/j.1365-246X.2012.05388.x.
Crameri, F., Magni, V., Domeier, M., Shephard, G.E., Chotalia, K., Cooper, G., Eakin, et al., 2020. A transdisciplinary and community-driven database to unravel subduction zone initiation. Nat. Commun. 11, 1-14.
Davaille, A., Smrekar, S.E., Tomlinson, S., 2017. Experimental and observational evidence for plume-induced subduction on Venus. Nat. Geosci. 10, 349–355.
Gerald, K.C., Gurevitch, A.B., Fedorenko, V., Simonov, O., 1998. Demise of the siberian plume: paleogeographic and paleotectonic reconstruction from the prevolcanic and volcanic record, North-Central Siberia. Int. Geol. Rev. 40, 95–115. https://doi.org/10.1080/00206819809465200.
Gerya, T.V., 2010. Introduction to Numerical Geodynamic Modelling. Cambridge University Press.
Gerya, T.V., 2013. Three-dimensional thermomechanical modeling of oceanic spreading initiation and evolution. Phys. Earth Planet. Inter. 214, 35–52.
Gerya, T., Meilick, F.I., 2011. Geodynamic regimes of subduction under an active margin: effects of rheological weakening by fluids and melts. J. Metamorph. Geol. https://doi.org/10.1111/J.1525-1314.2010.00904.X.
Gerya, T.V., Stern, R.J., Baes, M., Sobolev, S.V., Whattam, S.A., 2015. Plume-induced subduction initiation triggered Plate Tectonics on Earth. Nature 527, 221–225.
Gulcher, A.J.P., Gerya, T.V., Montesi, L.G.J., Munch, J., 2020. Corona structures driven by plume-lithosphere interactions and evidence for ongoing plume activity on Venus. Nat. Geosci. 13, 547–554.
Gurnis, M., Hall, C., Lavier, L., 2004. Evolving force balance during incipient subduction. Geochem. Geophys. Geosyst. 5. https://doi.org/10.1029/2003GC000681.
Herzberg, C., Gazel, E., 2009. Petrological evidence for secular cooling in mantle plumes. Nature 458, 619–622.
Hall, C., Gurnis, M., Sdrolias, M., Lavier, L.L., Müller, R.D., 2003. Catastrophic initiation of subduction following forced convergence across fracture zones, Earth Planet. Sci. Lett. 212, 15–30.
Hansen, V.L., 2009. Subduction origin on early Earth: a hypothesis. Geology 35, 1059–1062.
Holt, A.F., Royden, L.H., Becker, T., Faccenna, C., 2018. Slab interactions in 3-D subduction settings: The Philippine Sea Plate region. Earth Planet. Sci. Lett. 489, 72–83.
Ishikawa, T., Nagaishi, K., Umino, S., 2002. Boninitic volcanism in the Oman ophiolite: implications for the thermal condition during transition from spreading ridge to arc. Geology 30, 899–902.
Ito, K., Kennedy, G.C., 1971. An experimental study of the basalt-garnet granulite-eclogite transition, The Structure and Physical Properties of the Earth's Crust. Geophys. Monogr. Ser. 14, edited by J. G. Heacock, pp. 303-314, AGU, Washington, D. C.
Kerr, A.C., 2003. Oceanic plateaus, The Crust. Treatise on Geochemistry 3, 537–565.
Koptev, I.A., Cloetingh, S., Kovacs, I., Gerya, T., Ehlers, T.A., 2021. Controls by rheological structure of the lithosphere on the temporal evolution of continental magmatism: Inferences from the Pannonian Basin system. Earth Planet. Sci. Lett. 565,. https://doi.org/10.1016/j.epsl.2021.116925 116925.
Lebrun, J.-F., Lamarche, G., Collot, J.-Y., 2003. Subduction initiation at a strike-slip plate boundary: The Cenozoic Pacific-Australian plate boundary, south of New Zealand. J. Geophys. Res. 108, 2453. https://doi.org/10.1029/2002JB002041.
Li, X., Kind, R., Yuan, X., et al., 2004. Rejuvenation of the lithosphere by the Hawaiian plume. Nature 427, 827–829. https://doi.org/10.1038/nature02349.
Long, X., Yuan, C., Sun, M., Kröner, A., Zhao, G., Wilde, S., Hu, A., 2011. Reworking of the Tarim Craton by underplating of mantle plume-derived magmas: Evidence from Neoproterozoic granitoids in the Kuluketage area, NW China. Precambrian Res. 187 (1–2), 1–14.
Nikolaeva, k., Gerya, T.V., Marque, F.O., 2010. Subduction initiation at passive margins: Numerical modeling. J. Geophys. Res. 115, doi: 10.1029/2009JB006549.
O'Neill, C., Marchi, S., Zhang, S., Bottke, W., 2017. Impact-driven subduction on the Hadean Earth. Nat Geosci. 10, 793–797. https://doi.org/10.1038/ngeo3029.
Ranalli, G., 1995. Rheology of the Earth. Springer.
Regenauer-Lieb, K., Yuen, D.A., Branlund, J., 2001. The initiation of subduction: criticality by addition of water? Science 19, 578–580.
Revillon, S., Hallot, E., Arndt, N.T., Chauvel, C., Duncan, R.A., 2000. A complex history for the Caribbean Plateau: petrology, geochemistry, and geochronology of the Beata Ridge, South Hispaniola. J. Geol. 108, 641–661.
Rodriguez, M., Arnould, M., Coltice, N., Soret, M., 2021. Long-term evolution of a plume-induced subduction in the Neotethys realm. Earth Planet. Sci. Lett. 561,. https://doi.org/10.1016/j.epsl.2021.116798 116798.
Schilling, J.-G., 1991. Fluxes and excess temperatures of mantle plumes inferred from their interaction with migrating mid-ocean ridges. Nature 352, 397–403.
Sinton, C.W., Duncan, R.A., Storey, M., Lewis, J., Estrada, J.J., 1998. An oceanic flood basalt province within the Caribbean plate. Earth Planet. Sci. Lett. 155, 221–235.
Sobolev, S.V., Sobolev, A., Kuzmin, D., et al., 2011. Linking mantle plumes, large igneous provinces and environmental catastrophes. Nature 477, 312–316. https://doi.org/10.1038/nature10385.
Sobolev, S.V., Brown, M., 2019. Surface erosion events controlled the evolution of plate tectonics on Earth. Nature 570, 52–57.
Stern, R.J., Gerya, T.V., 2018. Subduction initiation in nature and models: a review. Tectonophysics 746, 173–198.
Stern, R.J., 2004. Subduction initiation: spontaneous and induced, Earth planet. Sci. Lett. 226, 275–292.
Stern, R.J., Dumitru, T.A., 2019. Eocene initiation of the Cascadia subduction zone: A second example of plume-induced subduction initiation? Geosphere 15, 659–681.
Toth, J., Gurnis, M., 1998. Dynamics of subduction initiation at preexisting fault zones. J. Geophys. Res. 103, 18053–18067.
Trela, J., Gazel, E., Sobolev, A.V., Moore, L., Bizimis, M., Jicha, B., et al., 2017. The hottest lavas of the Phanerozoic and the survival of deep Archaean reservoirs. Nat. Geosci. 10, 451–455.
Turcotte, D., Schubert, G., 1982. Geodynamics: Applications of Continuum Physics to Geological Problems. John Wiley, New York, p. 450.
Ueda, K., Gerya, T.V., Sobolev, S.V., 2008. Subduction initiation by thermal–chemical plumes: numerical studies. Phys. Earth Planet. Int. 171, 296–312.
Von Hagke, C., Philippon, M., Avouac, J.-P., Gurnis, M., 2016. Origin and time evolution of subduction polarity reversal from plate kinematics of Southeast Asia. Geology 44, 659–662.
Whattam, S.A., Stern, R.J., 2014. Late Cretaceous plume-induced subduction initiation along the southern margin of the Caribbean and NW South America: the first documented example with implications for the onset of plate tectonics. Gondwana Res. 27. https://doi.org/10.1016/j.gr.2014.07.011.
Whittaker, J.M., Afonso, J.C., Materton, S., Mueller, R.D., Wessel, P., Williams, S.E., Seton, M., 2015. Long-term interaction between mid-ocean ridges and mantle plumes. Nature Geosci. 8, 479–483.
Wie, X., Xu, Y.-G., Feng, Y.-X., Zhao, J.-X., 2014. Plume-lithosphere interaction in the generation of the Tarim large igneous province, NW China: Geochronological and geochemical constraints. Am. J. Sci. 314, 314–356.
Wilson, J.T., 1966. Did the Atlantic close and then re-open?. Nature 211, 676–681.
Zhong, X., Li, Z.-H., 2019. Forced subduction initiation at passive continental margins: Velocity-driven versus stress-driven. Geophys. Res. Lett. 46, 11054–11064. https://doi.org/10.1029/2019GL084022.
Zhong, X., Li, Z.-H., 2020. Subduction initiation during collision-induced subduction transference: Numerical modeling and implications for the Tethyan evolution. J. Geophys. Res. 125, e2019JB019288. https://doi.org/10.1029/2019JB019288.
Zhou, x., Li, Z-H., Gerya, T.V., Stern, R.J., 2020. Lateral propagation–induced subduction initiation at passive continental margins controlled by preexisting lithospheric weakness, Sci. Adv., Doi: 10.1126/sciadv.aaz1048.